Soft Matter

Optimizing the Accuracy of Viscoelastic Characterization with AFM Force-Distance Experiments in the Time and Frequency Domains

Journal:	*Soft Matter*
Manuscript ID	SM-ART-10-2022-001331.R1
Article Type:	Paper
Date Submitted by the Author:	22-Nov-2022
Complete List of Authors:	McCraw, Marshall; The George Washington University, Mechanical and Aerospace Engineering Uluutku, Berkin; The George Washington University, Mechanical and Aerospace Engineering Solomon, Halen; The George Washington University, Mechanical and Aerospace Engineering Anderson, Megan; The George Washington University, Mechanical and Aerospace Engineering Sarkar, Kausik; The George Washington University, Mechanical & Aerospace Engineering Solares, Santiago; The George Washington University, Mechanical and Aerospace Engineering

Optimizing the Accuracy of Viscoelastic Characterization with AFM Force-Distance Experiments in the Time and Frequency Domains

*Marshall R. McCraw, Berkin Uluutku, Halen D. Solomon, Megan S. Anderson, Kausik Sarkar, and Santiago D. Solares**

Department of Mechanical and Aerospace Engineering, The George Washington University School of Engineering and Applied Science, Washington, District of Columbia, USA

*Corresponding Author: Santiago D. Solares – ssolares@gwu.edu

KEYWORDS: Atomic force microscopy; viscoelasticity; material properties; force spectroscopy; information theory; optimal experiment design.

Abstract

Atomic Force Microscopy (AFM) force-distance (FD) experiments have emerged as an attractive alternative to traditional micro-rheology measurement techniques owing to their versatility of use in materials of a wide range of mechanical properties. Here, we show that the range of time dependent behaviour which can reliably be resolved from the typical method of FD inversion (fitting constitutive FD relations to FD data) is inherently restricted by the experimental parameters: sampling frequency, experiment length, and strain rate. Specifically, we demonstrate that violating these restrictions can result in errors in the values of the parameters of the complex modulus. In the case of complex materials, such as cells, whose behaviour is not specifically understood *a priori*, the physical sensibility of these parameters cannot be assessed and may lead to falsely attributing a physical phenomenon to an artifact of the violation of these restrictions. We use arguments from information theory to understand the nature of these inconsistencies as well as devise limits on the range of mechanical parameters which can be reliably obtained from FD experiments. The results further demonstrate that the nature of these restrictions depends on the domain (time or frequency) used in the inversion process, with the time domain being far more restrictive than the frequency domain. Finally, we demonstrate how to use these restrictions to better design FD experiments to target specific timescales of a material's behaviour through our analysis of a polydimethylsiloxane (PDMS) polymer sample.

1. Introduction

The field of mechanobiology has provided powerful insight into the rich behavior of soft, biological materials[1–6]. Of particular interest is rheological analysis. Due to the amorphous structure and active restructuring of living matter, measuring mechanical behaviors across a wide

range of timescales has allowed researchers to probe contributions of individual biopolymers in orchestrating the cell's bulk behavior. This work has provided an important lens for investigating drug-cell interaction and disease progression, for instance[7–15]. Many measurement techniques have been implemented to meet these needs – typically by mechanically stimulating the surface, or even sub-surface, with micro-pipette tips or colloidal particles manipulated with magnetic, optical, or mechanical systems[6–9,15–18]. Additional techniques based on Atomic Force Microscopy (AFM) and more generally, Scanning Probe Microscopy (SPM), have been used due to their uniquely versatile range of *in vitro* measurements and their non-destructive / minimally invasive nature[2,3,19–24].

In AFM, the surface of a material is interrogated using a probe affixed to the end of a cantilevered beam. Sharp probes (several nanometers wide) are used to measure the topography of the surface with sub-nanometer resolution by either dragging or tapping the probe across the surface. The probe can additionally be indented into the surface of the material, providing a simultaneous measurement of the depth of penetration and the force applied to the surface. In some cases, using larger probes (several microns wide) is desirable to obtain higher quality data at a lower spatial resolution. Using theories of contact mechanics such as that of Hertz, Sneddon, JKR, or DMT, one can obtain quantitative estimates of the elastic modulus of the material, provided that the geometry of the tip is known[25–33]. The complex modulus can be obtained using viscoelastic contact theories such as Ting's model or that of Lee and Radok[34–36]. Further details of these models can be found in exceptional detail in the literature[37–40].

Though unified through contact mechanics, many different AFM techniques exist to measure the complex modulus. Keeping with tradition, creep tests are commonly performed and provide a highly reliable method of obtaining the exponential relaxation of a material[21,41–46]. While in contact with the material, an additional harmonic excitation can be applied at set frequencies or in a frequency sweep, such as a chirp waveform, in a way that resembles Dynamic Mechanical Analysis[47–51]. Although creep or oscillatory based measurements can provide direct measurements of the relaxation modulus and complex modulus, respectively, they take several seconds to reliably probe the response of the material at long timescales. Additional measurements involving the harmonic excitation of the cantilever at, or close to, either its first or simultaneously, its second resonance frequency also exist. These methods provide the additional convenience of simultaneous acquisition of the surface topography and the complex modulus; however, the moduli obtained from these experiments are restricted to the operating frequency(ies) of the cantilever oscillation[24,52–54].

Though the maximum range of timescales that can be accessed from alternative techniques such as colloidal particle microrheology are similar to those in AFM, AFM typically operates in a smaller subset of this range whereas microrheological techniques take advantage of the entire range[7,14,49,55]. Recent work has sought to close this gap by utilizing the wideband nature of thermal oscillations[56–58]. Still, the most common viscoelastic characterization technique among AFM practitioners is the force-indentation (or force-distance, FD) experiment. Due to its simplicity and short duration, FD experiments are an attractive option for those seeking high throughput data acquisition to probe the heterogeneities inherent in biological materials[22,59]. As the previously mentioned AFM techniques typically take longer to perform, the amount of data that can be obtained from an experiment on sensitive, active materials like cells is limited compared to FD curves[22,60,61].

Such experiments have provided great insight into the detailed mechanical heterogeneities of cells[62] and have also allowed the investigation into cellular morphogenesis[63,64], mechanotransduction[65], motility[66], apoptosis[67], metastasis[68], and many other interesting phenomena[69–71]. Though AFM experiments have contributed significantly to many advancements

in biophysical understanding, the AFM as a device is extremely sensitive to deviations in its operating parameters which can skew results by several orders of magnitude[72]. Here, we will attempt to address how the experiment length, sampling frequency, and rate of indentation can be tailored to avoid such sensitivities in FD experiments. We will begin by deriving a simplified theoretical model for FD experiments, treating the material as a generalized Maxwell model. Using this model, we will first demonstrate the limitations of FD experiments in uniquely determining the set of model parameters that define the theoretical material. Following this, we will use arguments from information theory to understand the cause of these limitations and how to use them to optimally design FD experiments.

We present a brief graphical summary of the results in Fig. 1 below. One first needs to establish the maximum range of timescales governing the mechanical response(s) of interest. In the case of well-defined materials, one can use the literature for reference; however, for novel materials we suggest performing creep or relaxation experiments: one short experiment with maximal sampling and one long with maximal length. These experiments can then be used to obtain the smallest (τ_{min}) and largest (τ_{max}) relaxation times of a material and thus guide the selection of the experiment length (t_f) and sampling frequency ($1/\Delta t$) for use with FD experiments for the various viscoelastic inversion methods described in this manuscript, whether in the time domain (which includes two cases for the evaluation of the convolution between the stress/strain input and the viscoelastic functions) or in the frequency domain. One can additionally use these boundaries as a guide in data analysis to avoid overfitting.

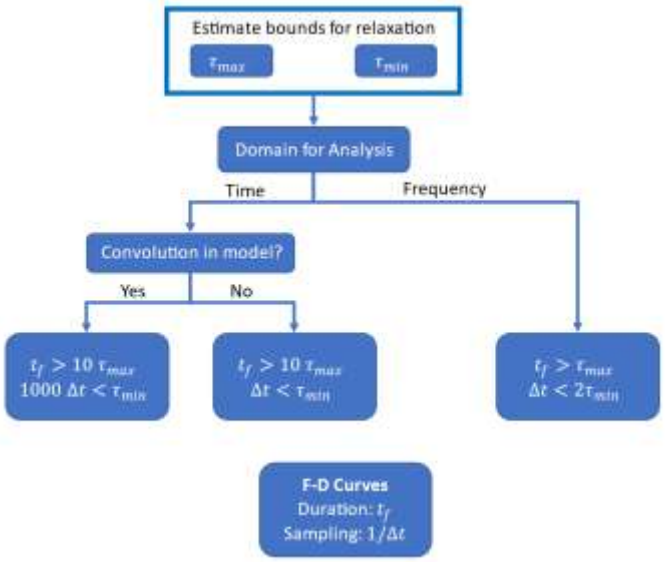

Figure 1: The range of time-dependent mechanical behavior that can be captured with an AFM FD experiment is generally limited by the length of the experiment t_f and the sampling frequency, or sampling period Δt. The specific limitation depends on the domain used in analyzing the data, either in the time domain or the frequency domain. One convenient way of informing FD experiments to capture these behaviors is to first obtain an estimate or a measurement (with a creep test) of the shortest and longest relaxation times τ_{min} and τ_{max} of a material.

2. Theoretical Background

In force-indentation experiments, the surface of the material is indented with the AFM probe while the indentation depth h and the resulting interaction force f are recorded in a way that is analogous to macro-scale tensile and compression test experiments. Using contact mechanics, one can relate the force and indentation in terms of a constitutive stress-strain equation which, for the case of a linear viscoelastic material, is generally a convolution integral as shown in Eqn. 1 and 1a[34–36,38–40,73,74]. Here, the terms α and β depend on the geometry of the AFM probe and can be found in further sources[22,26,35–38,40].

$$\sigma(t) = \int du\ Q(t-u)\varepsilon(u) \tag{1}$$

$$\frac{f(t)}{\alpha} = \int du\ Q(t-u)h^{\beta}(u) \tag{1a}$$

$$Q(\omega) = \frac{\sigma(\omega)}{\varepsilon(\omega)} = \frac{f(\omega)}{\alpha\ h^{\beta}(\omega)} \tag{2}$$

In the state-of-the-art, the viscoelastic modulus Q can then be obtained by first assuming a functional form for Q and then fitting the specific constitutive equation to the obtained force-indentation or stress-strain data in what we will refer to as the time domain approach[21,22,75–79]. Alternatively, one can use certain integral transforms, for which the convolution theorem is valid, to 'undo' the convolution and directly obtain the modulus from the transformed force-indentation data without prescribing a functional form to Q as seen in Eqn. 2 (here, we will use the modified Fourier transform with the notation $f(\omega)$ denoting the transform of f)[80,81]. While this 'frequency domain approach' allows an independence from model prescription, obtaining a model-based parameterization is often necessary for communication and comparison purposes. Thus, just as is done in the time domain approach, models for $Q(\omega)$ can be chosen and then fit to the transformed data.

While these methods offer straightforward solutions for obtaining parameterized descriptions of viscoelastic materials, their accuracy and reliability has recently been questioned[79,82]. Specifically, the time domain approach often yields unphysical or even conflicting values of the model parameters which depend on the initialization of the fitting algorithm[83]. Furthermore, a recent work by Vemaganti *et al* demonstrates that relaxation times can only be reliably obtained from stress relaxation experiments if they are less than 20% of the total experiment length[84]. Despite these inconsistencies in the model parameters, the fitted FD curves in the time domain often are in close agreement with the data and require detailed inspection to validate their physical sensibility. However, such an approach would be impractical in high throughput applications which often involve several 1000's of separate force curves within a single measurement.

Although not an exhaustive list, researchers tend to choose from Maxwell, Kelvin-Voigt, power-law, and fractional calculus-based models for the parametrization of the viscoelastic modulus[21,22,75–77,85]. Here, we will focus specifically on the generalized Maxwell model Q_{GM} as well as its special case, the standard linear solid (SLS), as seen in Fig. 2b and 2a, respectively. The generalized Maxwell model is mathematically defined by Eqn. 3 and 3a for the time and frequency domains, respectively (note that the modified Fourier domain representation is used in Eqn. 3a; further details can be found in the appendix). As seen in Fig. 2b, the generalized Maxwell model is comprised of a series of N 'Maxwell arms' in parallel with a single elastic element G_e. In the

special case $N = 1$, the model reduces to an SLS. Each arm has a spring element contributing an elasticity G_n and a dashpot (damper) element contributing a viscosity μ_n. The ratio of these arm components gives a characteristic relaxation time $\tau_n = \mu_n/G_n$ which governs the rate at which the stress in the n^{th} arm relaxes, with larger values corresponding to slower stress relaxation and vice-versa. By increasing the number of Maxwell arms N, one can describe a material with an intricate relaxation process. For example, a two-armed generalized Maxwell model was used to describe the 'fast' and 'slow' cytoskeletal rearrangement of cancer cells from stress-relaxation experiments[86].

$$Q_{GM}(t) = G_e\delta(t) + \sum_n^N \left[G_n\delta(t) - \frac{G_n}{\tau_n} e^{-\frac{t}{\tau_n}} \right] \tag{3}$$

$$Q_{GM}(\omega) = G_e + \sum_n^N \left[G_n - \frac{G_n}{1 + \frac{\tau_n}{\Delta t}\left(1 - \frac{e^{-i\omega}}{1.001}\right)} \right] \tag{3a}$$

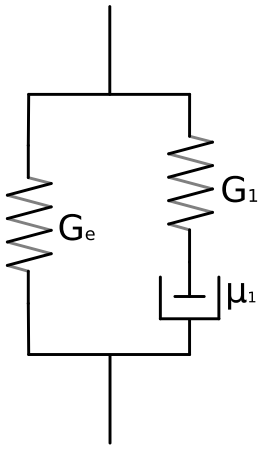

a) Standard Linear Solid Model

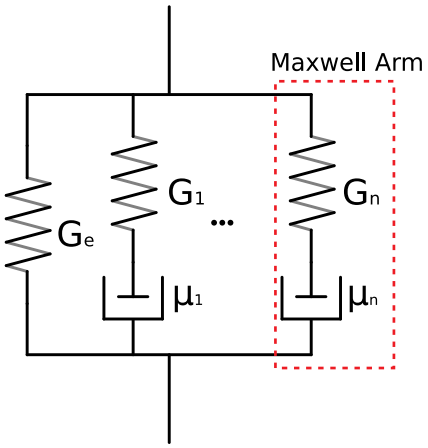

b) Generalized Maxwell Model

Figure 2: a) illustrations of a Standard Linear Solid (SLS) model and b) a generalized Maxwell (GM) model comprised of an arbitrary number of Maxwell arms, seen in dashed red.

As previously mentioned, we have found that the behavior of the generalized Maxwell model is relatively insensitive to changes in its parameter set $\boldsymbol{\theta}$ (i.e., G_e, G_1, τ_1 for an SLS). In the time domain, for instance, while a model fitted to a force-indentation curve may agree with the true data obtained from an experiment, the fitted values of $\boldsymbol{\theta}$ may vary significantly compared to the true values for the material. Such discrepancies are demonstrated in Fig. 3a where 100 generalized Maxwell models were fit to a simulated force-indentation curve (seen in blue). Although there are a few fits (seen in grey) which visually disagree with the true force-indentation data, the average (seen in red) follows the data quite well. If this were representative of a typical characterization experiment of the simulated material, the averaged data would be considered to have successfully described the material due to its agreement with the data. However, the discrepancies in the resulting fitted $\boldsymbol{\theta}$'s become apparent when plotting the storage and loss moduli (real and imaginary parts of $Q(\omega)$) for the fits, their average, and the data as seen in Fig. 3b and 3c, respectively. In Fig. 4, we see that values of the relaxation times (inverse of the frequency index of the peak in the loss modulus) disagree by 1-2 orders of magnitude between the fits and the data. Furthermore, as models with N between 1 and 4 were fit to the data, models with different numbers of relaxation times seem to equally describe the same force-indentation behavior in the time domain, despite the qualitative differences in the physics. As a result of this insensitivity to the number of relaxation times, the common practice for materials to be fitted with an arbitrary N, raises questions regarding overfitting the data and regarding fitting the data to incorrect physical behaviors. Although the comparison of the storage and loss moduli of the fits and the material seems to allow a more accurate assessment of the fit accuracy, such data is not directly obtained from the time domain fitting approach, thus making this assessment impossible if one fits in the time domain. However, the results suggest that the frequency domain approach should offer an advantage in more accurately parameterizing materials from force-indentation data.

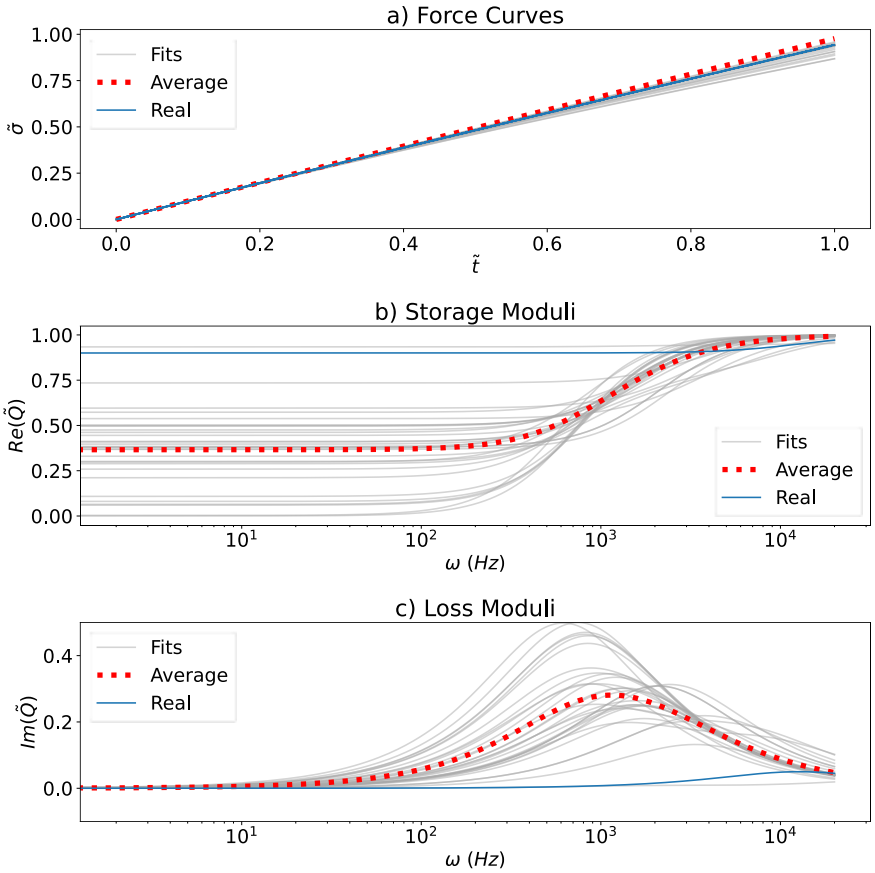

Figure 3: a) 100 randomly initialized (N between 1 and 4) fit attempts (grey) to a simulated force-indentation curve (N=1) (blue) with the average behavior of the fit attempts shown in dashed red. B) Storage moduli for each parameter set obtained from fitting and averaging. C) Loss moduli for each parameter set obtained from fitting and averaging.

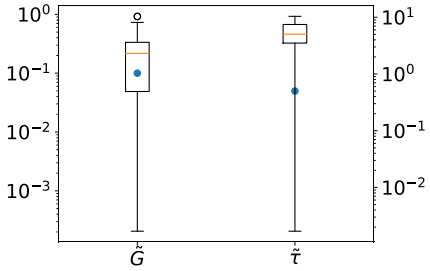

Figure 4: Values of the true model parameters (blue dots) from the model (blue curves in Fig. 3) plotted with the distribution of fitted parameters as box and whisker plots. As alluded to in Fig. 3, the modulus (magnitude of the response) is mostly recovered; however, the relaxation time is vastly overestimated.

3. Analysis

a. Insensitivity of the l^2 Norm

To compare the capabilities of these two approaches in determining an accurate $\boldsymbol{\theta}$ for a material, we will first use simplified, theoretical cases, treating force-indentation curves as linear strain inputs $h^{\beta}(t) = \varepsilon(t) \approx \varepsilon_0\, t$. While the indentation in AFM experiments is not typically linear, the 'strain' factor h^{β} in the contact mechanics models often closely follows a line as seen in the technical appendix. With this simplification, the stress-strain behavior for the linearized force-indentation model can be obtained by solving the Volterra integral in Eqn. 1 for the given strain $\varepsilon(t) = \varepsilon_0\, t$ and modulus $Q(t) = Q_{GM}(t)$. We further express both the time t and the relaxation times τ_n as fractions of the full experiment length t_f as well as normalize each arm elasticity G_n by the glassy (or instantaneous) modulus $G_g = G_e + \sum G_n$ to remove the dependence on G_e (the equilibrium modulus) and thus, reduce the dimensionality of $\boldsymbol{\theta}$. A similar dimensional analysis was performed for the modified Fourier domain representation of the modulus, yielding $\widetilde{Q}(\omega)$ where Δt denotes the sampling timestep of the experiment and 1.001 is the typical radial term used in the discrete modified Fourier transformation of FD curves[81]. One should note that an equivalent non-dimensionalization could be performed by scaling the timescales by the inverse of the strain rate, ε_0. Thus, the findings that are obtained from the analysis of the equations scaled by t_f are equivalent to those scaled by $1/\varepsilon_0$. The resulting dimensionless equations for the corresponding observables in both the time (stress $\tilde{\sigma}$) and frequency (modulus $\widetilde{Q}$) domains are given in Eqn. 4 and 4a; however, refer to the technical appendix for more thorough derivations. Using these models, simulated datasets $\tilde{\sigma}_{obs}$ and $\widetilde{Q}_{obs}$ can be generated for various values of $\boldsymbol{\theta}$ with the addition of Gaussian white noise with a standard deviation s equal to 0.1% of the full scale of the data. Hence, the simulated datasets are represented as $\tilde{\sigma}_{obs} = \tilde{\sigma} + P_N(0, s^2)$ and $\widetilde{Q}_{obs} = \widetilde{Q} + P_N(0, s^2)$, where $P_N(0, s^2)$ denotes a normal distribution sample with average equal to zero and variance s^2. Then, the $\boldsymbol{\theta}$ which describes the simulated data can be obtained through fitting the relevant model by minimization of the l^2 norm between the data ($\tilde{\sigma}_{obs}$ or $\widetilde{Q}_{obs}$) and the model 'prediction' ($\tilde{\sigma}$ or $\widetilde{Q}$), as defined in Eqn. 5 and 5a.

$$\tilde{\sigma}(t) = \frac{f(t)}{\alpha\, \varepsilon_0\, G_g\, t_f} = \tilde{t} + \sum_{n}^{N} \tilde{G}_n \tilde{\tau}_n \left(1 - e^{-\frac{\tilde{t}}{\tilde{\tau}_n}}\right) - \tilde{G}_n \tilde{t} \tag{4}$$

$$\tilde{Q}(\omega) = \frac{Q(\omega)}{G_g} = 1 - \sum_{n}^{N} \frac{\tilde{G}_n}{1 + \frac{\tilde{\tau}_n}{\Delta t}\left(1 - \frac{e^{-i\omega}}{1.001}\right)} \tag{4a}$$

$$l_{\tilde{t}}^2(\boldsymbol{\theta}) = \sum_{\tilde{t}} [\tilde{\sigma}(\tilde{t}, \boldsymbol{\theta}) - \tilde{\sigma}_{obs}(\tilde{t})]^2 \tag{5}$$

$$l_{\omega}^2(\boldsymbol{\theta}) = \sum_{\omega} \left[\tilde{Q}(\omega, \boldsymbol{\theta}) - \tilde{Q}_{obs}(\omega)\right]^2 \tag{5a}$$

The successful identification of $\boldsymbol{\theta}$ from a dataset is dependent on the structure of the l^2 norm; for example, if the norm has multiple local minima, an optimization algorithm may falsely identify one of these points as the true minimum. Furthermore, if the surface of the l^2 norm encompasses regions of $\boldsymbol{\theta}$ for which the values of the norm are below the machine precision level,

the computer will not be able to reliably distinguish between $\boldsymbol{\theta}$'s in these areas and the algorithm will also be unable to continue advancing towards the minimum[87].

In a mathematically simpler power-law viscoelastic model, it was recently demonstrated that the structure of the l^2 norm contained many local minima which resulted in frequent misidentifications of $\boldsymbol{\theta}$[83]. In Fig. 5a and 5b, we show the surfaces of the norm for both the time l_t^2 and frequency l_ω^2 domain models for a wide range of parameter space around the true minimum ($\tilde{G}_{1_{obs}} = 0.5, \tilde{\tau}_{1_{obs}} = 0.5$). Although these two-dimensional models do not have any local minima, the regions of flattened topography with values below the machine precision level introduce the possibility of stagnant optimization algorithms. Specifically, a large valley formation occurs around the minimum of the time domain model as seen in Fig. 5a. This valley encompasses a large range of possible values for the elasticity $\tilde{G}_1$ and relaxation time $\tilde{\tau}_1$, especially considering the normalization of these parameters, thus implying that parameters in this range offer no discernible change in the behavior of the model in the context of a force-indentation curve, from the perspective of the computer[87]. The variability of the fit results seen in Fig. 3 and the sensitivity to the initialization of the optimizer can then be understood as outcomes of this flatness in the l^2 surfaces.

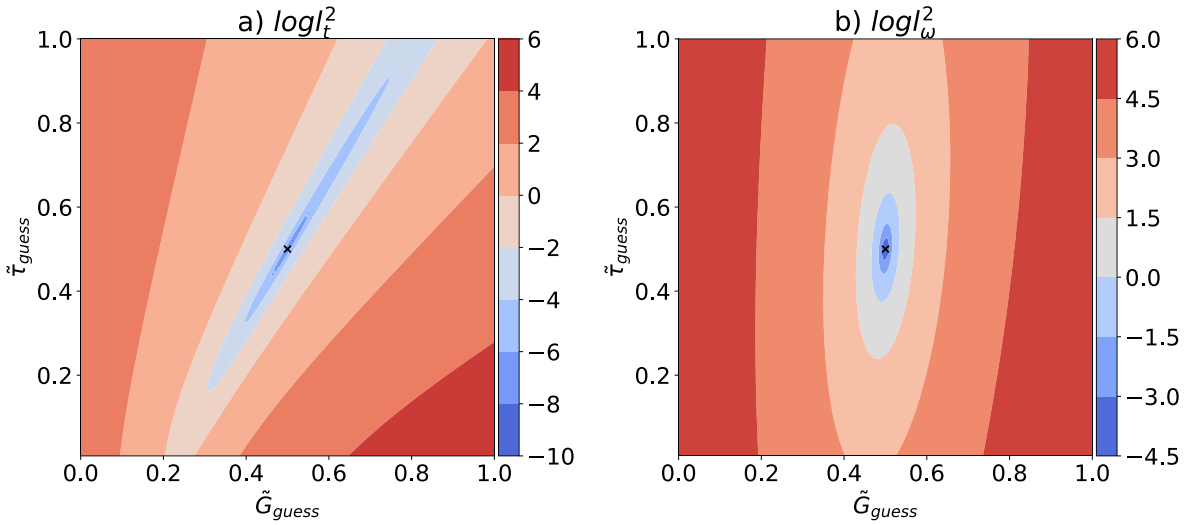

Figure 5: Surfaces of the l^2 norm for both the a) time and b) frequency domain models for a material with $\tilde{G}_{1_{obs}} = 0.5$ and $\tilde{\tau}_{1_{obs}} = 0.5$ (true values indicated on the plots with an X).

As the valley in the l_t^2 norm extends towards larger values of $\tilde{\tau}_1$, one can expect that arms with relaxation times that are comparable to the length of the experiment or close to the inverse strain rate ($\tilde{\tau}_n$ close to 1) will contribute a negligible amount to the model behaviour (since they have negligible effect on the norm). The functional form of the model in the time domain permits such a behavior as the term $1 - e^{-\tilde{t}/\tilde{\tau}_n}$ will remain small for most of the experiment. As the arm behavior is further scaled by the product of the modulus and the relaxation time $\tilde{G}_n\tilde{\tau}_n$, then, in the case where the relaxation time is large, the behavior of the arm is dominated by this product, allowing for errors in $\tilde{\tau}_n$ to be offset by inversely proportional errors in $\tilde{G}_n$, thus explaining the valley formed in the l_t^2 norm.

The norm in the frequency domain offers a contrast to the time domain norm, as seen in Fig. 5b. Here, a single, well-defined minimum in the parameter space is surrounded by a convex, highly curved surface, thus indicating that the model in the frequency domain is more amenable

to successful optimization attempts, even in the presence of considerable noise. Furthermore, the region of the parameter space that is below the machine precision level is confined to the area immediately around the true minimum, therefore, the problem of optimizers being unable to advance before reaching the true minimum is not present.

Although it may seem counterintuitive that these two representations of the same physics have differing behaviors when optimizing a fit, the finding is of a similar essence as the use of integral transforms in solving ordinary differential equations (ODEs). In the case of ODEs, certain integral transforms change the functional form of the equation allowing direct algebraic solutions to the equations. Here, the integral transforms change the functional form of the model in the time domain to a function that has greater sensitivity to its model parameters. A further analogy can be taken from support vector machines, which commonly apply transformations to the space of the dataset to arrive in a final space which specifically amplifies the differences between the global features of the data.

b. Information Theory

As we have discussed, the unreliability of the optimization can be attributed to the flatness of the l^2 norm, which itself can be attributed to the insensitivity of the model behavior with respect to $\boldsymbol{\theta}$. One might then question the case when the l^2 norm is completely flat for all values of $\boldsymbol{\theta}$. In this case, the parameters of the model would not control the description of the data as different values of $\boldsymbol{\theta}$ would describe the same phenomena with equal validity. In other words, the information provided by the data would be completely useless in identifying the optimal values of $\boldsymbol{\theta}$. In most cases the challenges may not be as drastic, but nevertheless, a robust procedure is necessary to ensure a proper fit for this particular parameter inversion problem. To fully quantify the information provided by a dataset about $\boldsymbol{\theta}$, we turn to information theory.

Here, we will use the log likelihood and the D-optimality criterion to assess how experimental conditions impact the information gathered about the optimal $\boldsymbol{\theta}$ of a material to then better design force-indentation experiments that would allow the user to obtain more meaningful data. While we will now present an informal description and motivation for the use of these two metrics, further details can be found in the technical appendix and more rigorous derivations and formal motivations can be found in the relevant literature[84,88–93].

First, consider representing the probability $P(\tilde{\sigma}_{obs}(\tilde{t}_0)|\boldsymbol{\theta})$ of correctly fitting the time domain model $\tilde{\sigma}$ at a single instant in time $\tilde{t}_0$ to a measured force-indentation curve $\tilde{\sigma}_{obs}$. As the noise in $\tilde{\sigma}_{obs}$ is assumed to follow a Gaussian process with standard deviation s, $P(\tilde{\sigma}_{obs}(\tilde{t}_0)|\boldsymbol{\theta})$ can then also be given as a Gaussian distribution as seen in Eqn. 6. Then, assuming the individual probability distributions for fitting each instant in time are independent and identically distributed, the probability (or likelihood) of correctly fitting the entire force-curve can be given as the product of the individual probability distributions for every instant in time. As the quality of the model's description of the data increases, so does the likelihood of proper fitting. Coincidentally, minimizing the l^2 norm with respect to $\boldsymbol{\theta}$ is equivalent to maximizing the likelihood with respect to $\boldsymbol{\theta}$. Hence the optimal parameter set is often referred to as the maximum likelihood estimate (MLE) of $\boldsymbol{\theta}$[94,95]. For the sake of convenience, the logarithm of the likelihood product is used, thus resulting in the log likelihood $L(\tilde{\sigma}_{obs}|\boldsymbol{\theta})$ (Eqn. 7 and 7a).

$$P(\tilde{\sigma}_{obs}(\tilde{t}_0)|\boldsymbol{\theta}) = \frac{1}{\sqrt{2\pi s^2}} e^{-\frac{\left(\tilde{\sigma}(\tilde{t}_0,\boldsymbol{\theta}) - \tilde{\sigma}_{obs}(\tilde{t}_0)\right)^2}{2s^2}} \tag{6}$$

$$L(\tilde{\sigma}_{obs}|\boldsymbol{\theta}) = \sum_{\tilde{t}} -\frac{\log(2\pi s^2)}{2} - \frac{\left(\tilde{\sigma}(\tilde{t},\boldsymbol{\theta}) - \tilde{\sigma}_{obs}(\tilde{t})\right)^2}{2s^2} \tag{7}$$

$$L\left(\tilde{Q}_{obs}|\boldsymbol{\theta}\right) = \sum_{\omega} -\frac{\log(2\pi s^2)}{2} - \frac{\left(\tilde{Q}(\omega,\boldsymbol{\theta}) - \tilde{Q}_{obs}(\omega)\right)^2}{2s^2} \tag{7a}$$

$$J(\boldsymbol{\theta}_{MLE})_{i,j} = \left[-\partial_{\theta_i}\partial_{\theta_j} L(\tilde{\sigma}_{obs}|\boldsymbol{\theta})\right]_{\boldsymbol{\theta}=\boldsymbol{\theta}_{MLE}} \tag{8}$$

$$J(\boldsymbol{\theta}_{MLE})_{i,j} = \left[-\partial_{\theta_i}\partial_{\theta_j} L\left(\tilde{Q}_{obs}|\boldsymbol{\theta}\right)\right]_{\boldsymbol{\theta}=\boldsymbol{\theta}_{MLE}} \tag{8a}$$

As previously stated, the flatness, or curvature of the l^2 norm allows us to build an insight into how to quantify the information contained within a dataset. Again, if the l^2 norm surface is entirely flat, changes in $\boldsymbol{\theta}$ will not alter the model's description of the data – therefore, the data provides no information about the optimal value of $\boldsymbol{\theta}$, given as $\boldsymbol{\theta}_{MLE}$. Conversely, if the l^2 norm, or equivalently the log likelihood, is highly curved in the vicinity of $\boldsymbol{\theta}_{MLE}$, then, the dataset is considered to contain a large amount of information about the $\boldsymbol{\theta}_{MLE}$. Thus, the curvature of the log likelihood in the vicinity of $\boldsymbol{\theta}_{MLE}$ seems to be a sensible metric to quantify the information that the dataset contains about $\boldsymbol{\theta}_{MLE}$. Indeed, the matrix of mixed second partial derivatives $J(\boldsymbol{\theta}_{MLE})_{i,j}$ of the log likelihood, evaluated at $\boldsymbol{\theta}_{MLE}$ (Eqn. 8 and 8a) is a commonly used measurement to quantify this information and is referred to as the Observed Fisher Information matrix. Various elements of $J(\boldsymbol{\theta}_{MLE})_{i,j}$ can be used to quantify the information contained in a dataset[88,89]. Here, we consider the determinant $\det(J)$ of the matrix, referred to as the D-optimality criterion. Of course, while we provided the motivation and informal derivations of $\det(J)$ and $L(\tilde{\sigma}_{obs}|\boldsymbol{\theta})$ using the example of force-indentation curves (time domain), the results are equally valid for the frequency domain model of the modulus.

i. Time Domain

First, we consider the behavior of the information $\det(J)$ of a force-indentation experiment on a material with a single relaxation time $\tilde{\tau}_1$ (SLS, Fig. 2a) in the time domain. In Fig. 6a, the distribution of $\det(J)$ increases exponentially as a function of the dimensionless time, obtaining its maximum value at the end of the experiment (a longer experiment provides more information than a shorter one, generally speaking, since it allows greater probing of the material behaviour, assuming a uniform strain rate). While the relaxation time is not mathematically restricted to be shorter than the length of the experiment, it is evident that the information available for larger relaxation times is much diminished in comparison to those relaxation times that are shorter. This is as expected, since such relaxation times would not be reached in shorter experiments, and therefore, their effects could not be observed. Most noteworthy is the behavior of the information after $\tilde{\tau}_1$ exceeds $t_f/10$ as evidenced by the exponential decrease in the information calculated at the end of the experiment, seen in Fig. 6b. We can then deduce that relaxation times larger than $t_f/10$ do not contribute significantly to the behavior of the model (within an experiment of length t_f), a finding that is consistent with the flatness seen in the regions

of the contour maps of the l_t^2 norm for values of $\tilde{\tau} > 0.1$. A similar result was previously reported for stress-relaxation experiments wherein the information obtained about relaxation times exceeding $t_f/5$ was significantly diminished[84]. As the nondimensionalization of the timescales with respect to the experiment length is equivalent to normalizing by the inverse of the strain rate, it is evident that this upper bound can also be expressed as $1/10\ \varepsilon_0$. From here, we can see that exciting the material with a more abrupt strain input results in a more restricted upper bound as the experiment probes the shorter timescales of the material. By straining the material very slowly, the upper bound increases, allowing one to access the response of the material at larger timescales.

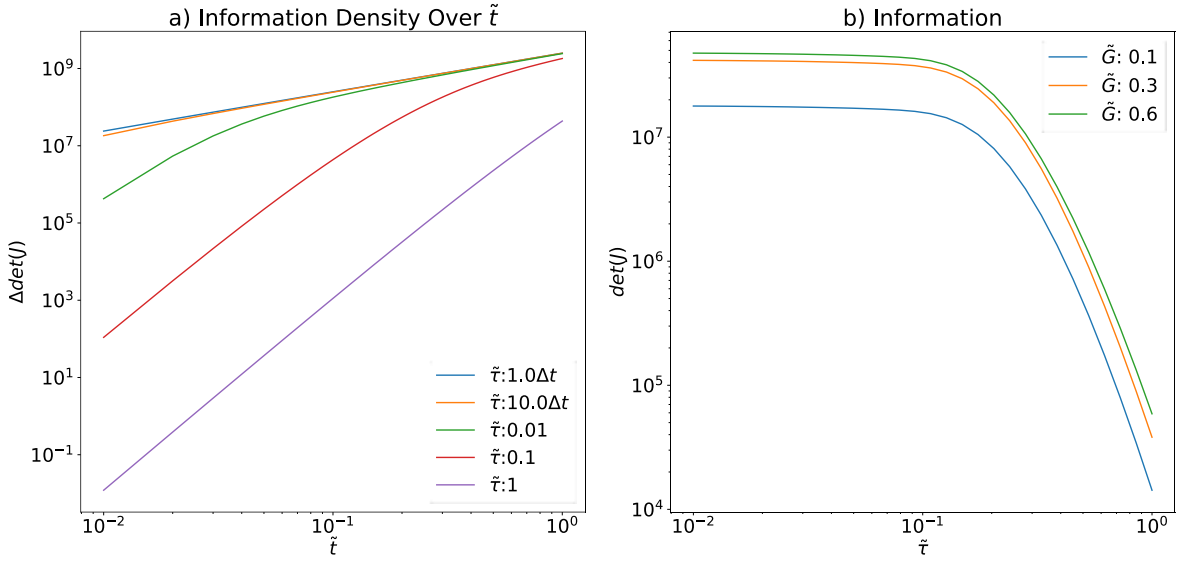

Figure 6: a) Distribution of information over the dimensionless time for SLS materials with various relaxation times. b) The behavior of the information as a function of the relaxation time for various moduli.

Conversely, as the relaxation time decreases, the information increases, indicating that shorter relaxation times will be easier to identify. However, as $\tilde{\tau}$ approaches the sampling timestep Δt of the experiment, this information gain stagnates. In this case, the relaxation process governed by $e^{-\tilde{t}/\tilde{\tau}_n}$ is not adequately sampled in the experiment and thus, relaxation processes that occur in a period shorter than the sampling frequency do not lead to a change in the behavior of the model. This behavior can be clearly seen in Fig. 7. Here, the stress response (Fig. 7b) of a material defined by the shear modulus in Fig. 7a is plotted in blue. Two 'experiments' are provided in green and red, using values of Δt and t_f which violate these boundaries. The green curves correspond to an experiment that is too short compared to the relaxation time (i.e. $t_f < \tilde{\tau}$) and thus, do not capture the viscoelastic relaxation of the material. The red crosses correspond to an experiment with a sampling period much larger than the relaxation time of the material (i.e. $\Delta t > \tilde{\tau}$) and thus, do not reflect the high frequency response of the material.

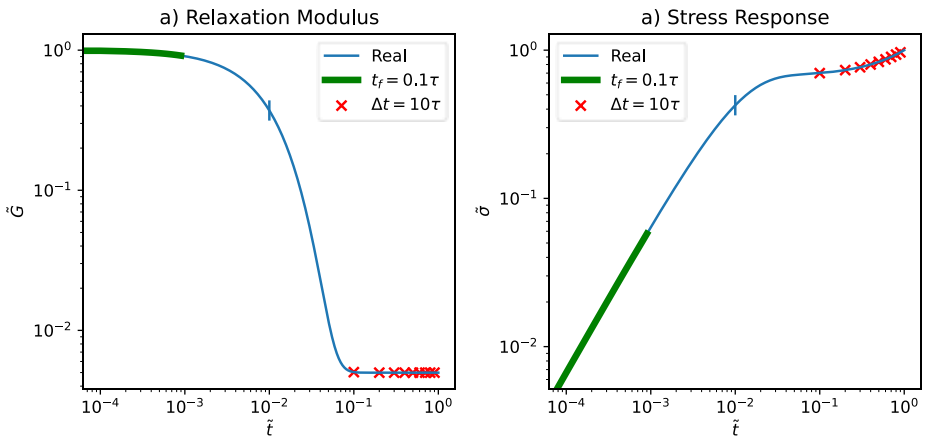

Figure 7: a) Relaxation modulus (step response) of the dimensionless model in the time domain and b) stress response of the model defined in a) to an arbitrary strain input. In both plots, the true value of the material is shown in blue with the location of the dimensionless relaxation time marked by a vertical blue line. The green curve indicates an experiment which is shorter than the relaxation time and thus unable to capture the dynamic behavior of the material. The red crosses correspond to an experiment with a sampling frequency that is too large compared to the relaxation time and thus does not capture the high frequency (short time) response of the material.

A further restriction can be placed on the lower bound of the relaxation time when the general convolution definition for the stress-strain or force-indentation relationship is used, such as in Eqn. 1 and 1a, rather than assuming a linearized excitation. In this case, as the data from the experiment is a discrete signal, the convolution operator is inherently discretized. However, approximating continuous convolutions like those in Eqn. 1 and 1a with a discretized convolution is only valid when the kernel Q and the input ε or h^{β} are band limited functions[95]. Of course, Q is not generally band limited; however, as shown in the technical appendix, Q can be approximately treated as being band limited only when the shortest relaxation time is several orders of magnitude greater than the sampling timestep of the experiment:

$$\tau_{min} > 1000\,\Delta t \tag{9}$$

To demonstrate how these restrictions impact the behavior of materials with multiple relaxation times, we first simulate the force-indentation behavior of a material with two relaxation times $\tilde{\tau}_1, \tilde{\tau}_2$ and two moduli $\tilde{G}_1, \tilde{G}_2$. We then assess the description of this data by a model with a single relaxation time (SLS) by calculating the normalized maximum log likelihood $L(\tilde{\sigma}_{obs}|\boldsymbol{\theta}_{MLE})$. In Fig. 8a and 8d, we plot $L(\tilde{\sigma}_{obs}|\boldsymbol{\theta}_{MLE})$ for various combinations of $\tilde{\tau}_1, \tilde{\tau}_2$ and $\tilde{G}_1, \tilde{G}_2$. As the difference between the two relaxation times $\tilde{\tau}_1, \tilde{\tau}_2$ of the material increases, the ability of the SLS model in describing the features of the data diminishes as evidenced by the decrease in $L(\tilde{\sigma}_{obs}|\boldsymbol{\theta}_{MLE})$. Of course, as $\tilde{\tau}_1$ and $\tilde{\tau}_2$ approach each other, the opposite is true as their behaviors can be equivalently treated as a single relaxation time. As seen in the wide distributions in $L(\tilde{\sigma}_{obs}|\boldsymbol{\theta}_{MLE})$, if the difference between $\tilde{\tau}_1$ and $\tilde{\tau}_2$ drops within 1-2 orders of magnitude, the likelihood that the data can be described by a single relaxation time is maximized. In such a case, the two nearly coincidental relaxation times would not be resolved from the analysis of the experimental data in the time domain. For example, consider the blue curve in Fig. 8a. Here, $\tilde{G}_1 =$

$\tilde{G}_2 = 0.5$, $\tilde{\tau}_1 = 0.001$s, and various values of $\tilde{\tau}_2$ are given along the x-axis of the figure. In this case, only values of $\tilde{\tau}_2 > 0.1$s can be distinguished in the time domain (i.e., only for values of $\tilde{\tau}_2 > 0.1$s is it possible to determine that having a single relaxation time in the model is insufficient to fit the data). To better illustrate this point, the data and the SLS fit associated with $\tilde{\tau}_2 = 0.01$s is provided in Fig. 8c. As expected from the preceding discussion, the two relaxation times cannot be determined, thus the SLS model adequately and more concisely describes the material.

A similar phenomenon occurs as one of the relaxation times approaches or surpasses the length of the experiment, or the inverse of the strain rate. Even if the two relaxation times are separated by several orders of magnitude (for instance $\tilde{\tau}_1 = 0.001, \tilde{\tau}_2 = 10$ as seen in the blue curve in Fig. 8a), the slower relaxation process will not be able to have a significant effect on the behaviour of the material during the experiment and thus, will not be detected in the experiment (since $\tilde{\tau}_2 = 10$ is ten times longer than the duration of the experiment). This explains why the curves in Fig. 8a and 8d rise after reaching a minimum when $\tilde{\tau}_2$ is approximately unity).

A further example can be seen in the orange log likelihood curve in Fig. 8a and the corresponding set of force curves seen in Fig. 8b. In this example, the relaxation times are separated by nearly three orders of magnitude; therefore, the insufficiency using single relaxation time in the model is readily identified in the time domain and one can easily conclude that SLS description of the data is inaccurate. An additional example is provided in Fig. 8d for the case when one of the moduli of the material is small compared to its total stiffness. Here, similar features of $L(\tilde{\sigma}_{obs}|\boldsymbol{\theta}_{MLE})$ are seen wherein the behaviors of the relaxation times are most noticeably different when they are separated by several orders of magnitude. However, as one of the moduli is smaller than for the previous example, the effects associated with this modulus are similarly negligible. Therefore, the magnitude of $L(\tilde{\sigma}_{obs}|\boldsymbol{\theta}_{MLE})$ for the SLS is significantly increased for most of the horizontal axis range in Fig. 8d when compared to Fig. 8a, thus suggesting that relaxation times should only be introduced when they are associated with moduli that are roughly equal in magnitude.

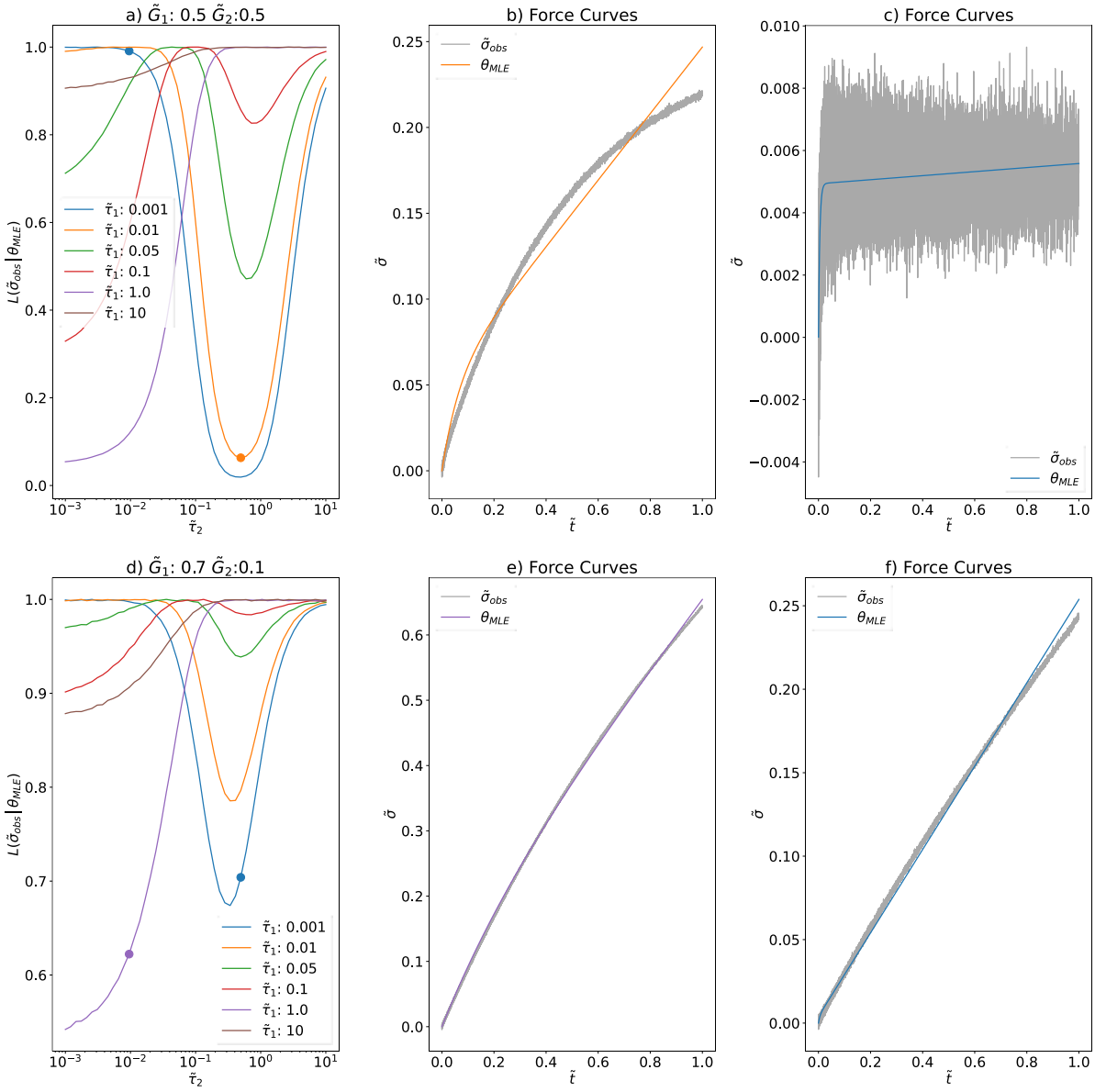

Figure 8: The maximum log likelihood $L(\tilde{\sigma}_{obs}|\boldsymbol{\theta}_{MLE})$ for an SLS description of a material with two relaxation times $\tilde{\tau}_1, \tilde{\tau}_2$ and $\tilde{G}_1, \tilde{G}_2$. a) shows $L(\tilde{\sigma}_{obs}|\boldsymbol{\theta}_{MLE})$ normalized to a 0-1 scale for a material given by $\tilde{G}_1 = \tilde{G}_2 = 0.5$ with various combinations of relaxation times. b) shows the force-indentation curve corresponding to the circular orange marker in Fig. 8a and the most likely SLS description. c) shows a similar correspondence for the circular blue marker in Fig. 8a. d) shows values of $L(\tilde{\sigma}_{obs}|\boldsymbol{\theta}_{MLE})$ normalized to a 0-1 scale for a material given by $\tilde{G}_1 = 0.7$ and $\tilde{G}_2 = 0.1$ ($\tilde{G}_1$ noticeably larger than $\tilde{G}_2$) for various relaxation times. e) shows a correspondence for the circular purple marker in Fig. 8d. f) shows a correspondence for the circular blue marker in Fig. 8d.

We can then conclude that for force-indentation curves in the time domain, relaxation times can most reliably be extracted when their values fall between Δt and $t_f/10$ (or equivalently $1/10\ \varepsilon_0$), when using a linearized force-indentation model as we have done in our example. If the

force-indentation relation is kept general (i.e., without specifying its form) and the (discretized) convolution definition is used, then the lower bound increases to about $1000\ \Delta t$. Furthermore, the presence of multiple relaxation times can only be determined if they are separated by at least 1-2 orders of magnitude and within the previously mentioned ranges. Additionally, the magnitude of the moduli of each Maxwell arm should be comparable and larger than the amplitude of the measurement noise. Similarly, as the magnitude of both the log likelihood and the information scale inversely with the square of the amplitude of the noise, the ability to determine these parameters drastically diminishes as the amount of noise increases. Violating these criteria introduces the possibility of fitting these parameters to artifacts unrelated to the material.

ii. Frequency Domain

A similar approach can be taken to determine the range of detectable relaxation times in the frequency domain. As was done in the time domain, we first assess the shape of the information distribution $\det(J)$ of a model with a single relaxation time as a function of frequency as seen in Fig. 9a. For relaxation times between the sampling timestep and the length of the experiment, the information increases until the frequency passes the relaxation frequency $\tilde{\omega}_r = 1/\tilde{\tau}$. After this point, the information slowly declines with frequency; however, this feature is an artifact of the normalization of $\tilde{Q}$ with respect to G_g since now all the models share a common behavior for frequencies greater than $1/\tilde{\tau}$.

The behavior of the information in $\tilde{Q}$ can be understood by investigating the behavior of the model as a function of frequency. Fig. 10 shows the storage and loss moduli of $\tilde{Q}$ for various values of $\tilde{\tau}$. The behavior of the storage modulus follows a sigmoidal-like transition between G_e and G_g whereas the loss modulus follows a shape similar to a Boltzmann distribution. As the locations of these features are controlled by $\tilde{\omega}_r$, increasing $\tilde{\tau}$ past the resolution of the frequency axis will cause these features to not be adequately sampled during the experiment as seen in the pink curves in Fig. 10a and 10b. As the resolution of the frequency axis is given as t_f, relaxation times that are longer than the length of the experiment will not be properly sampled. Therefore, we can understand the decaying behavior of the information for large values of $\tilde{\tau}$ as seen in Fig. 9b. Of course, this behavior is consistent with what is seen in the time domain; however, the decay is not as abrupt in the frequency domain compared with the time domain, as seen in Fig. 7b.

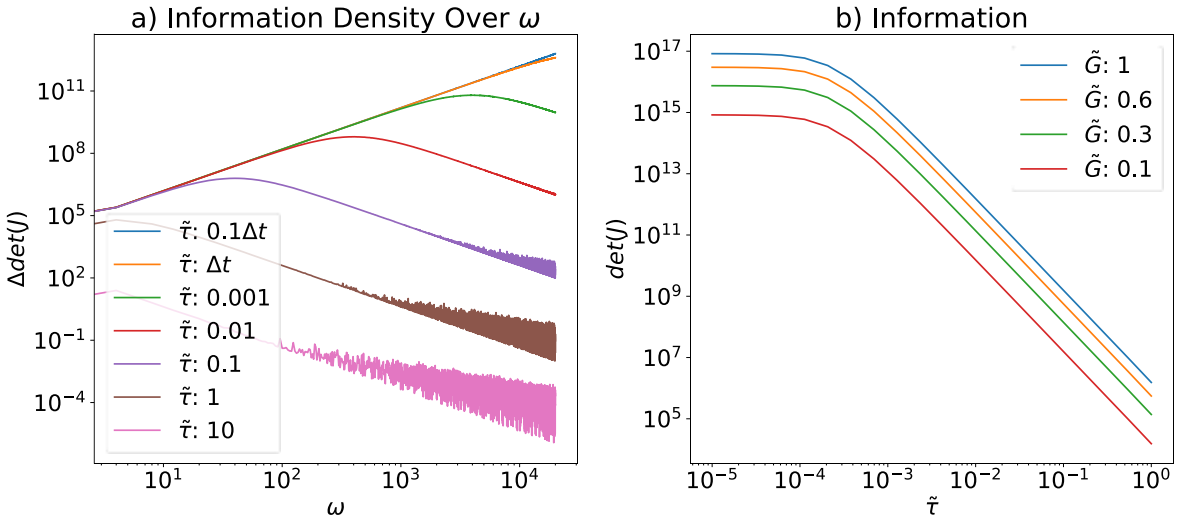

Figure 9: a) Distribution of information over the dimensionless time for SLS materials with various relaxation times with $\tilde{G} = 1$ (fluid-like materials). b) Behavior of the information as a function of the relaxation time for various moduli.

On the opposite end, as the relaxation time decreases, the magnitude of the information increases until it meets a stagnation point as also seen in the time domain. In this case, the location of the previously mentioned features of the storage and loss moduli shifts outside of the Nyquist band when $\tilde{\tau}$ decreases past $2\,\Delta t$. Therefore, relaxation times that happen faster than the length of the sampling window will not be obtained in the frequency domain. It is interesting to note that the model appears to correspond to two different 'elastic' solids when $\tilde{\tau}$ is outside of these detectable bounds. On one end, the material relaxes so quickly as to appear instantaneous – on the other, the material relaxes so slowly as to appear as if it doesn't relax at all. Both cases result in approximately flat storage and loss moduli with the flatness increasing as $\tilde{\tau}$ approaches either 0 or ∞[38].

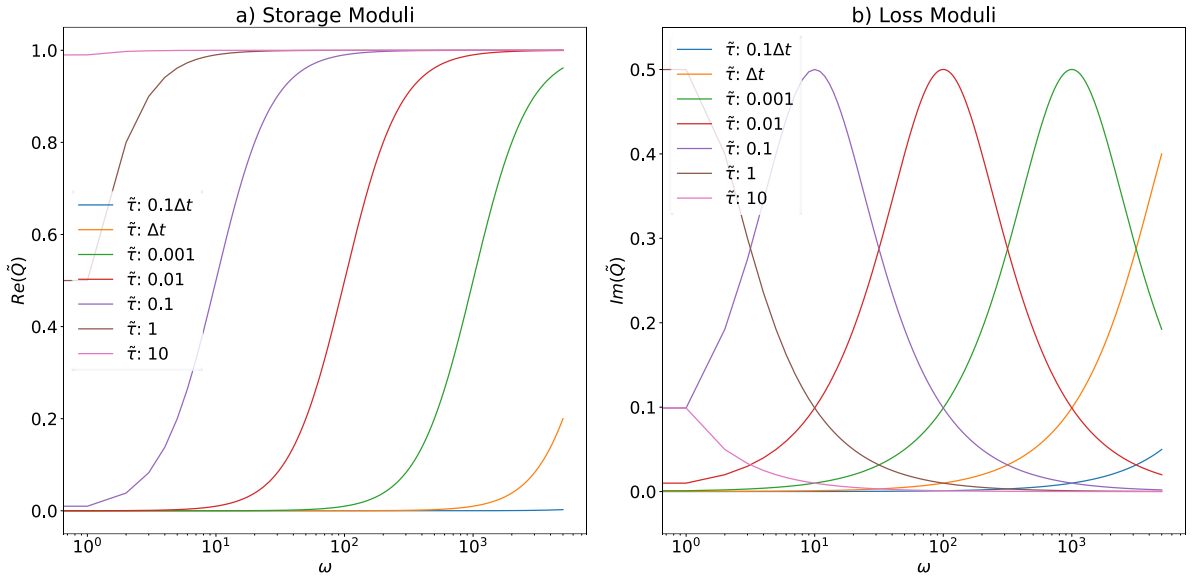

Figure 10: Behavior of the a) storage and b) loss moduli of the SLS model for various relaxation times with $\tilde{G} = 1$ (fluid-like materials). As stated in the text, the storage modulus behaves as a sigmoid, with its transition period being governed by the inverse of the relaxation time. The loss modulus follows a similar shape as a Boltzmann distribution, with its maximum value occurring at the inverse of the relaxation time.

It should be noted that $2\,\Delta t$ serves as an idealized lower limit for the detectable relaxation times. In practice, noise may obscure the behavior of the material at high frequencies. When deriving the model for $\widetilde{Q}$ that was used in obtaining these results, we used the explicit form of $\widetilde{Q}$ for a generalized Maxwell model, therefore avoiding taking the modified Fourier transform of the force-indentation curves (i.e., $\widetilde{Q}$ was not obtained from data, but instead from its analytical expression). We further assumed that the noise would be linearly additive to $\widetilde{Q}$; however, when calculating $\widetilde{Q}$ directly by inverting the force-indentation data, the noise does not follow a simple linear behavior. In the technical appendix we demonstrate that the expected value of the magnitude of the noise induced error in $\widetilde{Q}$ scales with the square of the amplitude of the noise and inversely with the square of the magnitude of the transformed strain as seen in Eqn. 10. As

the magnitude of the modified discrete Fourier transform of monotonically increasing linear-like inputs (as are typical in force-indentation experiments – further demonstrated in the appendix) rapidly diminishes at high frequencies, high frequency error is commonly observed when calculating $\widetilde{Q}$. This high frequency error can be thought of as noise with an amplitude, or standard deviation, which increases as a function of frequency. As mentioned before, since the information $\det(J)$ scales inversely with the square of the amplitude of the noise, we can expect that the increasing noise will result in a more rapid attenuation of the information at high frequencies and thus, it will impose greater restrictions on the lower limit of detectable relaxation times. To avoid this issue, one can use strain excitations that decay more slowly in the modified Fourier domain. Since these types of 'weakly decaying' spectra correspond to more slowly diverging excitations in the time domain, it is advantageous from a noise perspective to perform slower experiments. According to the results established in the time domain section, this also corresponds to decreasing the strain rate, thus increasing the upper bound of accessible relaxation times. Alternatively, a slower diverging signal has a wider bandwidth in the modified Fourier domain, thus allowing for a broader, more reliable characterization of the material response.

$$\delta_Q \sim \frac{s^2}{|\varepsilon(\omega)|^2} \tag{10}$$

As we did in the time domain, we will now assess the behavior of materials with multiple relaxation times in the frequency domain. We will again investigate the maximum log likelihood $L\left(\widetilde{Q}_{obs}\middle|\boldsymbol{\theta}_{MLE}\right)$ of an SLS model in describing a material with two relaxation times $\tilde{\tau}_1, \tilde{\tau}_2$. As seen in the same calculation done for the time domain, the SLS model can describe such a material only when the difference between $\tilde{\tau}_1$ and $\tilde{\tau}_2$ is small. However, unlike the time domain, the differences in $\tilde{\tau}_1$ and $\tilde{\tau}_2$ for which this single relaxation time approximation is valid are much smaller, indicating that one can more easily discern when additional relaxation times are needed in the model. In Fig. 11a and 11d, the peak-like distributions formed in $L\left(\widetilde{Q}_{obs}\middle|\boldsymbol{\theta}_{MLE}\right)$ indicate regions where the single relaxation time approximation is valid. Compared to the corresponding plots in the time domain seen in Fig. 8a and 8d, the distributions formed here are much narrower and larger in magnitude, again suggesting that the effects associated with the relaxation times are more pronounced in the frequency domain compared to the time domain. Such a behavior should be expected, however, as the number of distinct relaxation times is directly linked to the number of distinct peaks in the loss modulus.

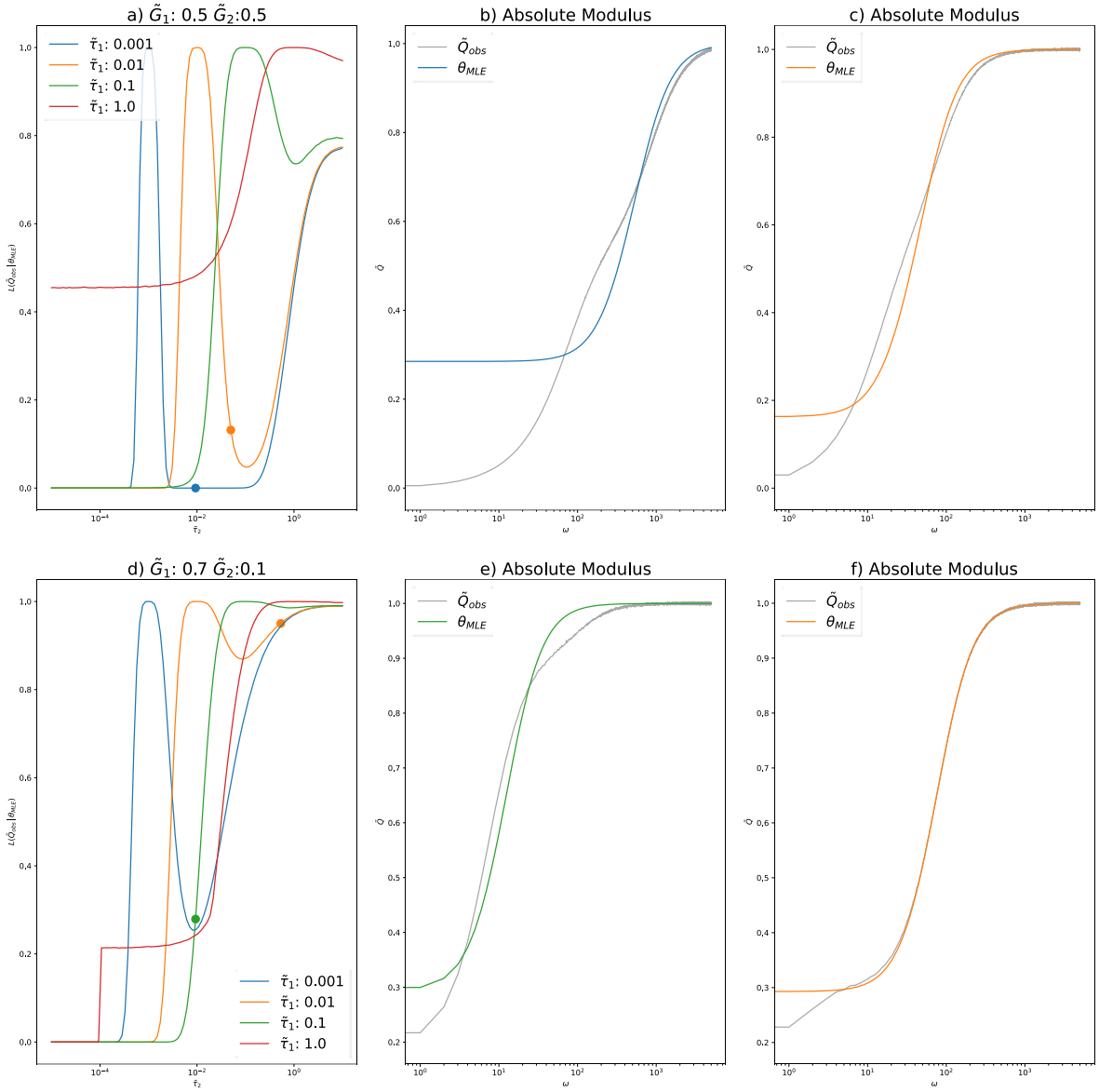

Figure 11: The maximum log likelihood $L(\tilde{Q}_{obs}|\boldsymbol{\theta}_{MLE})$ for an SLS description of a material with two relaxation times $\tilde{\tau}_1, \tilde{\tau}_2$ and $\tilde{G}_1, \tilde{G}_2$. a) shows $L(\tilde{Q}_{obs}|\boldsymbol{\theta}_{MLE})$ normalized to a 0-1 scale for a material given by $\tilde{G}_1 = \tilde{G}_2 = 0.5$ with various combinations of relaxation times. b) shows a correspondence between the circular blue marker in Fig. 11a and its associated absolute moduli for the material and the most likely SLS description. c) shows a similar correspondence between the circular orange marker in Fig. 11a. d) shows values of $L(\tilde{Q}_{obs}|\boldsymbol{\theta}_{MLE})$ normalized to a 0-1 scale for a material given by $\tilde{G}_1 = 0.7$ and $\tilde{G}_2 = 0.1$ for various relaxation times. e) shows a correspondence for the circular green marker in Fig. 11d. f) shows a correspondence for the circular orange marker in Fig. 11d.

As was done in Fig. 8, color-coded markers have been placed on top of the plots in Fig. 11a and 11d to correspond to individual plots of the behavior of the SLS description of various two-relaxation-time materials in the frequency domain. Consider first the blue marker in Fig. 8a: as the log likelihood is significantly reduced, we can imagine that the SLS model should not be able

to describe the material. Indeed, this is evident in Fig. 8b as the error in $\widetilde{Q}$ propagates across a few decades of frequency. Such an example illustrates very well the distinction between the frequency and time domains as here, we see that materials with relaxation times within an order of magnitude can be resolved whereas the time domain required 1-2 orders of magnitude of separation. Furthermore, we see that the magnitude of the normalized log likelihood approaches a value of 0 for a significant range of separation between the relaxation times. Such a feature was not present in the corresponding time domain plot. Further examples can be seen in Fig. 11c, e, and f.

We can thus observe that the frequency domain offers a significant advantage over the time domain in determining the parameters of generalized Maxwell models. Specifically, relaxation times between $2\,\Delta t$ and t_f can be individually determined, with the behaviour of multiple relaxation times being able to be resolved if they are separated by more than an order of magnitude. The results have been summarized in Table 1 below.

Table 1: Summarized description of the minimum and maximum relaxation times obtained from the time and frequency domain analysis of force-indentation experiments as well as the minimum resolution for which multiple relaxation times can be determined.

	$\boldsymbol{\tau_{min}}$	$\boldsymbol{\tau_{max}}$	$\boldsymbol{\Delta\tau_{min}}$
Time domain	Δt^*	$t_f/10$	2 orders of magnitude
Frequency domain	$2\,\Delta t^*$	t_f	1 order of magnitude

**Note that the lower bound for the time domain will increase by 3 orders of magnitude if the discrete convolution is used to calculate the force-indentation model. Additionally, the lower bound of the frequency domain will also increase in the presence of noise in the direct inversion of the force-indentation data.*

4. Demonstration with Experiments

We can now demonstrate how these criteria can be leveraged to better design force-indentation (FD) experiments to more accurately characterize a polydimethylsiloxane (PDMS) sample. In this demonstration, we will use AFM FD curves as well as uniaxial compression tests done on the macro-scale with a Universal Testing Machine (MTS) (see Methods section below). As the compression tests are performed by applying a linear strain input, the results of the previous sections should also apply. As a reminder, we have determined that in the time domain, one can only obtain relaxation times between the sampling timestep Δt and one tenth of the length of the experiment $t_f/10$. Within these bounds, multiple relaxation times can only be determined if they are separated by 2 decades of time and if they contribute similar values of their respective moduli. Alternatively, if one opts to use the frequency domain, the maximum range of detectable relaxation times increases to be between $2\Delta t$ and t_f and the required minimum spacing between multiple relaxation times decreases to a single decade.

Thus, to design an AFM experiment which maximizes the information obtained about the characteristic timescales of PDMS, we will first have to estimate the relaxation time(s) for the material using commonly accepted data. As the relaxation time of a material is roughly given as the ratio of its viscosity to its elasticity, we estimate the relaxation time of PDMS by dividing accepted values for its viscosity by its accepted modulus, given as $1\,kPa\,s$ and $1\,MPa$, respectively[96,97]. The resulting estimate for τ is then found to be $10^{-3}\,s$. Therefore, we specify our AFM experiment to have a sampling timestep of $2 * 10^{-5}\,s$ (the lower limit on this particular AFM instrument) and an experiment length of approximately $0.1s$. Additionally, the approach velocity was specified to give a strain rate of roughly $40\,\frac{\%}{s}$ (indentation normalized by probe

radius). Thus, the boundaries of accessible timescales from the AFM experiment are determined to be at most $2 * 10^{-5}\ s$ and $0.01s$ in the time domain, and at most $4 * 10^{-5}\ s$ and $0.1s$ in the frequency domain. However, it should be noted that if we use the general convolution definition for fitting the force-indentation curves in the time domain, the lower limit increases to only $0.02s$, about an order of magnitude larger than the characteristic timescale of PDMS. Additionally, these restrictions on the time domain analysis limit us to only characterize a single relaxation time. To utilize the full range of information available from the AFM experiment, one would have to assume a functional form for the indentation, which is hardly ideal, or simply use the frequency domain approach. To further extend the range of the timescales that can be obtained from this experiment, one would need to decrease the sampling rate and increase the length of each experiment. In the frequency domain, however, we can obtain τ values between $4 * 10^{-5}\ s$ and $0.1s$. Furthermore, since we can capture the behavior of multiple relaxation times separated by only a single decade, we can obtain a much greater resolution than compared to the time domain. For example, an experiment length of $0.1\ s$ allows the determination of, at most, four unique relaxation times – far greater than the single relaxation time obtained in the time domain. As the analysis performed here used *a priori* knowledge to estimate the relaxation time of PDMS, it might not reflect experimentation procedures on unmeasured materials. In these cases, we recommend to first use creep tests to determine a bound for the longest relaxation time of the material. Once this has been determined, the experiment can be designed around capturing this behavior using the guidelines in Table 1.

The macroscale mechanical tester used here is typically applied in much slower experiments as compared to the AFM, applying a strain rate of only $0.2\ \frac{\%}{s}$. As a result of the slower deformation rate, the sampling timestep was restricted to only $0.1s$ and the length of the experiment was around $10s$. Thus, we can expect that the macroscale experiment will yield a superb characterization of the low frequency values of Q (longer timescale relaxations) but will be unable to describe the expected $10^{-3}\ s$ relaxation time of the material.

Fig. 12a and 12b show the spectral averaged storage and loss moduli of the material obtained from direct modified Fourier inversion of the AFM force-indentation and MTS stress-strain curves corresponding to our established method[81]. The set of force-indentation and stress-strain curves can be seen in Fig. 12c and 12d. The values of the storage and loss moduli (dotted scatter plots) obtained from the two devices agree exceptionally well within the small frequency range of overlap. Furthermore, both of these results agree quite well with accepted values for the storage and loss modulus of PDMS[98]. As the Nyquist frequency limit of the macroscale MTS experiment is restricted to only 5 Hz, the observed behaviour of the PDMS is mostly elastic – having a flat storage modulus and negligible loss modulus. This feature was consistent when fitting both the time and frequency domain constitutive equations for the Maxwell model (Eqn. 3 and 3a) to the respective time and frequency domain data as can be seen in Table 2. Here, the Maxwell model parameters obtained from the fitting procedures indicate that PDMS is an elastic material with a modulus of ~$0.5MPa$ – in relatively good agreement with the accepted $\sim 0.9\ MPa$. Of course, we know PDMS to be viscoelastic; however, the MTS experiment was not able to probe the relevant timescales of this rate dependence due to its limited sampling timestep.

As existing dynamic mechanical analyses of PDMS have been limited to only a few hundred Hz, the plateauing behaviour of the storage modulus, a hallmark of Maxwell materials, is usually not fully captured as it is in the AFM data in Fig. 12a. In the presence of such restrictions on the acquisition of high frequency data, it is common to use power law models which fit the data well in the low frequency regime, but fail to capture the higher frequency plateau, if present. Like the MTS data, we fit Maxwell models (Eqn. 3 and 3a) to the time and frequency domain data obtained

from the AFM experiments. As a reminder, we had specified the sampling rate, experiment length, and linearized strain rate such that the estimated relaxation time of the PDMS falls within these boundaries. In the time domain, however, we chose to use the general convolution definition rather than assume a functional form for the indentation which resulted in a lower bound which was greater than this estimated time constant. As a result, the quantities identified from the time domain, although they agree with the force curves, do not agree with the frequency domain data. As we have come to expect, the frequency domain provides quantities which agree with the behavior of the material in both the time and frequency domains.

To further demonstrate the quality of this agreement, we have supplied the mean squared error between fitted force-indentation and stress-strain curves using the parameters obtained from both the time and frequency domain approaches with the AFM and MTS. As seen in these errors as well as in Fig. 12c and 12d, the qualitative behaviour of these curves agrees quite well, with the frequency domain tending to provide a slightly more optimal result than the time domain (note that the force curve for the frequency domain parameters was constructed using a high order polynomial fit to the data as the general convolution definition would not work for the relaxation time obtained from this parameter set). We can then conclude that due to the larger range of detectable timescales available in the spectral analysis of the AFM experiments, we are able to detect the viscoelastic nature of the material. Since the MTS experiment does not adequately interrogate the timescale of the rate-dependent behaviour of the PDMS, we are led to conclude that the material is elastic.

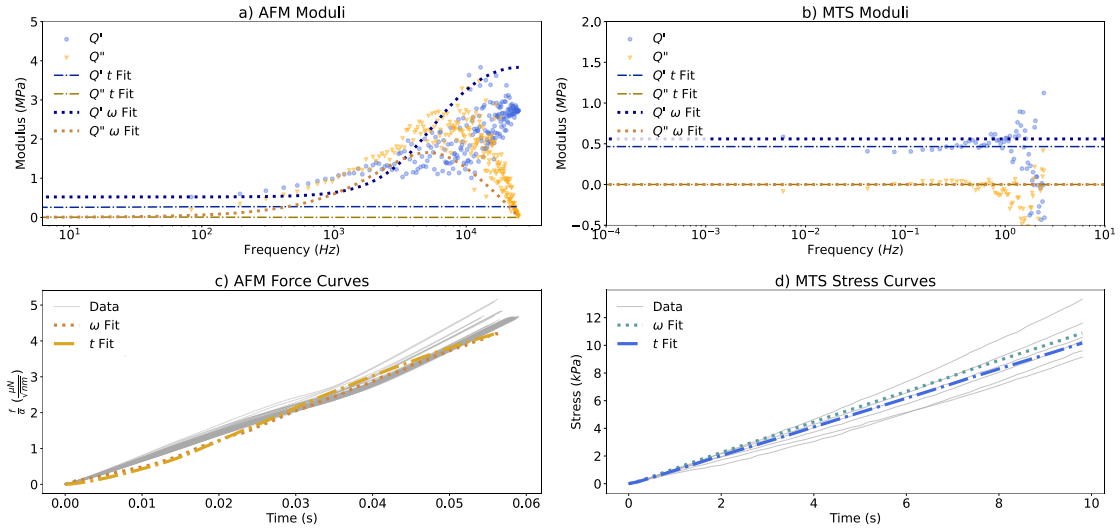

Figure 12: a) the spectral averaged storage (blue scatter) and loss (yellow scatter) moduli obtained from the direct inversion of the AFM force-indentation curves. b) The spectral averaged storage (blue scatter) and loss (yellow scatter) moduli obtained from the direct inversion of the MTS stress-strain curves. c) The set of force-indentation curves from the AFM experiment (grey) and corresponding time (dashes) and frequency (squares) domain fits. d) The set of stress-strain curves from the MTS experiment (grey) and corresponding time (dashes) and frequency (squares) domain fits.

Table 2: SLS parameters obtained from the characterization of PDMS using AFM and macroscale testing data in the time and frequency domain. We also include the ensemble averaged mean

squared error between the fitted force-indentation and stress-strain curves (parameters obtained from fitting in both time and frequency domains) and the data obtained from the experiments.

	$G_e\ (MPa)$	$G_1\ (MPa)$	$\tau_1(s)$	MSE in time fit
AFM t	0.0	0.3	0.06	$4 * 10^{-14}$
AFM ω	0.5	5.0	0.0002	$2 * 10^{-14}$
MTS t	0.6	0.0	0.02	$9 * 10^{6}$
MTS ω	0.5	0.0	0.9	$7 * 10^{6}$

5. Conclusions

Though AFM has shown itself to be incredibly useful for biomechanical research, significant care is required in both planning and evaluating experiments. As has been recently published, the results of AFM experiments can vary significantly through slight alterations of the experimental parameters, thus understanding how to better design experiments is a critical requirement in developing more robust experimental techniques[72]. As we have shown, the range of timescales that can be obtained from force curves analysed in the time domain is at best limited to be less than a tenth of the length of the experiment and more than the sampling period. Furthermore, the use of the general convolution definition with discrete data may lead to severe inaccuracies which can only be avoided by increasing the lower bound by roughly a factor of 1000. To provide more context, such a finding is of significant importance in high throughput force volume measurements where individual force curves are performed in less than $1 * 10^{-3}s$ with a sampling period on the order of $1 * 10^{-6}s$. In these cases, the discretized convolution will never yield accurate results. One way to avoid these issues could involve modulating the temperature of the sample, provided that it is stable under heating / cooling. Assuming time-temperature equivalence, one could effectively alter the timescale of a previously unobservable timescale by heating or cooling the sample[99]. Measurements targeting specific timescales could then be stitched together with those performed across a range of temperatures. Additionally, one could consider the portion of the FD experiment where the tip retracts from the sample. By doing so, one effectively extends the length of the experiment, allowing for the detection of larger relaxation times; however, great care is needed in maintaining the validity of the contact theories. We direct the readers to recent works on this topic[100,101].

Although we have demonstrated that performing this analysis in the frequency domain allows a much wider range of accessible timescales for the same experiment, we assumed that the noise, which stems from the time domain, would add linearly to the frequency domain. Such an assumption was necessary to simplify the analysis, but it is clear from the noise in the experimental data seen in Fig. 12, that this can cause serious issues. We further investigate the effects of idealized noise sources in the technical appendix, but a more rigorous analysis of the effects of more realistic noise sources would be beneficial to the community specifically in the measurement of materials with multiple distinct relaxation times spanning a wide frequency range. For instance, scaffolds for tissue engineering and cell culture are often constructed using dynamically associating polymers which are known to possess a number of distinct relaxation times ranging from low frequencies (binding kinetics) to high frequencies (chain dynamics / hydrodynamics if relevant)[102–105]. In these applications, it is essential to properly tailor the mechanics of these materials across all relevant timescales to best optimize for cell viability. We hope that this work provides guidance for AFM research in these fields.

We would like to remind readers that the results of our analysis are specific to the models that we have used. Though the GM model is capable of generically describing viscoelastic

behaviors, its applicability to *any arbitrary* viscoelastic material could be dubious. As our analysis covers materials with either one or two distinct relaxation times, it is important to consider that realistic materials can obey some sort of power law or fractional viscoelastic behavior with a distribution of closely packed relaxation times[39,46,73,75,85]. In these cases, GM and even SLS models often provide sufficiently good approximations of these more complicated behaviors. Thus, we argue that the results of our analysis can still be used, at least in a qualitative way, to guide FD experimentation on materials with closely distributed relaxation times. As power law, fractional viscoelastic, and GM models describe the same physics (creep, relaxation, recovery), one should expect there to be a correspondence between the results of this analysis in terms of the length of the experiment and the sampling frequency. Furthermore, the argument of band limitation in determining the validity of the discrete convolution operation will still hold for power law / fractional moduli. Of course, to quantitatively describe the correspondence between these classes of models, additional work is needed.

Future work on the optimization of AFM FD experiments should consider alternative functional forms of the strain excitation. Here, we considered only linearized strain inputs which closely model real FD experiments but can only be adjusted in terms of their strain rates. Specifically, impulse-like excitations may yield a broader interrogation of the timescales of the material. One could perhaps also express the problem as a functional optimization, seeking to obtain the strain input which maximizes an information functional. These types of advancements would allow the AFM to become a more robust rheological characterization tool.

6. Methods

A SYLGARD 184 Silicone Elastomer kit was used to prepare Polydimethylsiloxane (PDMS) following the standard procedure of mixing the base elastomer and the curing agent in a 10:1 mass ratio. The majority of the liquid was then poured into a flat-bottomed glass dish to a depth of 1 cm to be used for compression testing. The Atomic Force Microscopy (AFM) sample was made using 2 mL of the remaining liquid which was spin coated on a steel microscope sample disk at 100 rpm for 2 minutes. Both samples were then degassed and cured at room temperature for 24 hours.

A 10 mm biopsy punch was then used to extract 6 cylindrical samples from the glass dish. We then performed uniaxial unconfined compression testing (UUCT) with a Universal Testing Machine (MTS) (Applied Test Systems, Butler, PA, USA) on these samples using a 100 N load cell at a crosshead speed of 1 mm/min. The thickness of each sample was measured using a digital caliper with a sensitivity of 0.01 mm. The experimental stress was calculated as the applied force of the load cell divided by the cross-sectional area of the sample in direct contact with the UUCT device. Additionally, the strain was calculated as the ratio of the sample displacement to the original sample thickness.

AFM force spectroscopy measurements were then done in a room temperature environment filled with air with an MFP-3D (Asylum Research, Oxford Instruments, Santa Barbara, CA, USA) AFM using an ElectriCont-G (BudgetSensors, Izgrev, Sofia, Bulgaria) probe. The optical lever sensitivity was calibrated using the linear region of the repulsive part of a force curve performed on a freshly cleaned silicon wafer. The cantilever spring constant was determined to be 0.08617 N/m by thermal calibration using Sader's method[106]. 4 rounds of force spectroscopy experiments were performed on 4 different spots on the surface of the PDMS-coated steel disk. Each round of spectroscopy involved probing the surface of the sample 150 times within a confined region. Each force curve was specified with an approach velocity of

1.89 mm/s, a sampling frequency of 50 kHz, and a trigger force of 738.98 pN to stay within the small deformation criteria of contact mechanics. The probe was treated as a sphere with a radius of 25 nm as specified by the vendor information sheet.

Acknowledgements

M.R.M, K.S. and S.D.S. gratefully acknowledge support from the US National Science Foundation, under award CMMI-2019507. B.U. gratefully acknowledges support from the US Department of Energy, Office of Science, Basic Energy Sciences, under Award No. DE-SC0018041. M.S.A. and K.S. gratefully acknowledge support from the US National Science Foundation, under award CBET-2037849, and the ARCS Foundation Metro Washington Chapter.

References

1 A. X. Cartagena-Rivera, J. S. Logue, C. M. Waterman and R. S. Chadwick, *Biophysical Journal*, 2016, **110**, 2528–2539.
2 M. O. Krisenko, A. Cartagena, A. Raman and R. L. Geahlen, *Biochemistry*, 2015, **54**, 60–68.
3 C. Rotsch and M. Radmacher, *Biophysical Journal*, 2000, **78**, 520–535.
4 M. Prass, K. Jacobson, A. Mogilner and M. Radmacher, *Journal of Cell Biology*, 2006, **174**, 767–772.
5 N. Mandriota, C. Friedsam, J. A. Jones-Molina, K. V. Tatem, D. E. Ingber and O. Sahin, *Nat. Mater.*, 2019, **18**, 1071–1077.
6 B. R. Parry, I. V. Surovtsev, M. T. Cabeen, C. S. O'Hern, E. R. Dufresne and C. Jacobs-Wagner, *Cell*, 2014, **156**, 183–194.
7 B. A. Krajina, C. Tropini, A. Zhu, P. DiGiacomo, J. L. Sonnenburg, S. C. Heilshorn and A. J. Spakowitz, *ACS Cent. Sci.*, 2017, **3**, 1294–1303.
8 B. A. Krajina, B. L. LeSavage, J. G. Roth, A. W. Zhu, P. C. Cai, A. J. Spakowitz and S. C. Heilshorn, *Sci. Adv.*, 2021, **7**, eabe1969.
9 C. R. Jacobs, H. Huang and R. Y. Kwon, *Introduction to cell mechanics and mechanobiology*, Garland Science, New York, 2013.
10 G. Giubertoni, F. Burla, H. J. Bakker and G. H. Koenderink, *Macromolecules*, 2020, **53**, 10503–10513.
11 F. Di Lorenzo and S. Seiffert, *Macromolecules*, 2013, **46**, 1962–1972.
12 A. Aufderhorst-Roberts, W. J. Frith, M. Kirkland and A. M. Donald, *Langmuir*, 2014, **30**, 4483–4492.
13 T. Narita, K. Mayumi, G. Ducouret and P. Hébraud, *Macromolecules*, 2013, **46**, 4174–4183.
14 F. C. MacKintosh and C. F. Schmidt, *Current Opinion in Colloid & Interface Science*, 1999, **4**, 300–307.
15 J. C. Crocker, M. T. Valentine, E. R. Weeks, T. Gisler, P. D. Kaplan, A. G. Yodh and D. A. Weitz, *Phys. Rev. Lett.*, 2000, **85**, 888–891.
16 I. Huszár, Z. Mártonfalvi, A. Laki, K. Iván and M. Kellermayer, *Entropy*, 2014, **16**, 4322–4337.
17 Z. Mei, J. D. Treado, A. T. Grigas, Z. A. Levine, L. Regan and C. S. O'Hern, *Proteins*, 2020, **88**, 1154–1161.
18 T. Gisler and D. A. Weitz, *Phys. Rev. Lett.*, 1999, **82**, 1606–1609.
19 T. Majmudar, S. Balasubramanian, R. Magee, B. Gonik and A. Singh, *Journal of Biomechanics*, 2021, **128**, 110702.
20 C. Rianna and M. Radmacher, 2016.
21 Y. M. Efremov, T. Okajima and A. Raman, *Soft Matter*, 2020, **16**, 64–81.
22 R. Garcia, *Chem. Soc. Rev.*, 2020, **49**, 5850–5884.
23 P. D. Garcia and R. Garcia, *Nanoscale*, , DOI:10.1039/C8NR05899G.

24 S. Benaglia, C. A. Amo and R. Garcia, *Nanoscale*, 2019, **11**, 15289–15297.
25 H. Hertz, *crll*, 1882, **1882**, 156–171.
26 I. N. Sneddon, *International Journal of Engineering Science*, 1965, **3**, 47–57.
27 K. L. Johnson, *Contact Mechanics*, Cambridge University Press, 1st edn., 1985.
28 K. L. Johnson, *Proceedings of the Institution of Mechanical Engineers*, 1982, **196**, 363–378.
29 D. Maugis, *Contact, Adhesion and Rupture of Elastic Solids*, Springer Berlin Heidelberg, Berlin, Heidelberg, 2000.
30 B. V. Derjaguin, V. M. Muller and Yu. P. Toporov, *Journal of Colloid and Interface Science*, 1975, **53**, 314–326.
31 D. Tabor, *Reviews of Physics in Technology*, 1970, **1**, 145–179.
32 D. Maugis, *Journal of Colloid and Interface Science*, 1992, **150**, 243–269.
33 J. A. Greenwood and J. B. P. Williamson, *Proc. R. Soc. Lond. A*, 1966, **295**, 300–319.
34 T. C. T. Ting, *Journal of Applied Mechanics*, 1966, **33**, 845–854.
35 T. C. T. Ting, *Journal of Applied Mechanics*, 1968, **35**, 248–254.
36 E. H. Lee and J. R. M. Radok, *Journal of Applied Mechanics*, 1960, **27**, 438–444.
37 I. N. Sneddon, *Fourier transforms*, Dover Publications, New York, 1995.
38 R. M. Christensen, *Theory of viscoelasticity*, Dover Publications, Mineola, N.Y, 2nd ed., 2003.
39 D. R. Bland, *The theory of linear viscoelasticity*, Dover Publications, Inc, Mineola, New York, 2016.
40 J. M. Golden and G. A. C. Graham, *Boundary Value Problems in Linear Viscoelasticity*, Springer Berlin Heidelberg, Berlin, Heidelberg, 1988.
41 C. Braunsmann, R. Proksch, I. Revenko and T. E. Schäffer, *Polymer*, 2014, **55**, 219–225.
42 G. Moeller, *J. Polym. Sci. B Polym. Phys.*, 2009, **47**, 1573–1587.
43 E. M. Darling, S. Zauscher and F. Guilak, *Osteoarthritis and Cartilage*, 2006, **14**, 571–579.
44 H. W. Wu, T. Kuhn and V. T. Moy, *Scanning*, 2006, **20**, 389–397.
45 S. Moreno-Flores, R. Benitez, M. dM Vivanco and J. L. Toca-Herrera, *Nanotechnology*, 2010, **21**, 445101.
46 S. Hiratsuka, Y. Mizutani, A. Toda, N. Fukushima, K. Kawahara, H. Tokumoto and T. Okajima, *Jpn. J. Appl. Phys.*, 2009, **48**, 08JB17.
47 R. E. Mahaffy, C. K. Shih, F. C. MacKintosh and J. Käs, *Phys. Rev. Lett.*, 2000, **85**, 880–883.
48 E. Ueda, X. Liang, M. Ito and K. Nakajima, *Macromolecules*, 2019, **52**, 311–319.
49 J. Alcaraz, L. Buscemi, M. Grabulosa, X. Trepat, B. Fabry, R. Farré and D. Navajas, *Biophysical Journal*, 2003, **84**, 2071–2079.
50 C. A. Grant, M. A. Phillips and N. H. Thomson, *Journal of the Mechanical Behavior of Biomedical Materials*, 2012, **5**, 165–170.
51 F. Oulevey, N. A. Burnham, G. Gremaud, A. J. Kulik, H. M. Pollock, A. Hammiche, M. Reading, M. Song and D. J. Hourston, *Polymer*, 2000, **41**, 3087–3092.
52 A. B. Churnside, R. C. Tung and J. P. Killgore, *Langmuir*, 2015, **31**, 11143–11149.
53 R. C. Tung, J. P. Killgore and D. C. Hurley, *Review of Scientific Instruments*, 2013, **84**, 073703.
54 P. A. Yuya, D. C. Hurley and J. A. Turner, *J. Appl. Phys.*, 2008, **104**, 074916.
55 P. C. Cai, B. A. Krajina, M. J. Kratochvil, L. Zou, A. Zhu, E. B. Burgener, P. L. Bollyky, C. E. Milla, M. J. Webber, A. J. Spakowitz and S. C. Heilshorn, *Soft Matter*, 2021, **17**, 1929–1939.
56 C. Martinez-Torres, A. Arneodo, L. Streppa, P. Argoul and F. Argoul, *Appl. Phys. Lett.*, 2016, **108**, 034102.
57 E. Lyapunova, A. Nikituk, Y. Bayandin, O. Naimark, C. Rianna and M. Radmacher, Tomsk, Russia, 2016, p. 020046.
58 X. Xiong, S. Guo, Z. Xu, P. Sheng and P. Tong, *Phys. Rev. E*, 2009, **80**, 061604.
59 Yu. M. Efremov, A. I. Shpichka, S. L. Kotova and P. S. Timashev, *Soft Matter*, 2019, **15**, 5455–5463.

60 S. Jesse, R. Vasudevan, L. Collins, E. Strelcov, M. Okatan, A. Belianinov, A. Baddorf, R. Proksch and S. Kalinin, *Annual review of physical chemistry*, 2014, **65**, 519–36.
61 M. Chyasnavichyus, S. L. Young and V. V. Tsukruk, *Jpn. J. Appl. Phys.*, 2015, **54**, 08LA02.
62 A. Cartagena and A. Raman, *Biophysical Journal*, 2014, **106**, 1033–1043.
63 D. E. Ingber, *Cell*, 1993, **75**, 1249–1252.
64 D. J. Montell, *Science*, 2008, **322**, 1502–1505.
65 N. Wang, J. P. Butler and D. E. Ingber, *Science*, 1993, **260**, 1124–1127.
66 D. Yamazaki, S. Kurisu and T. Takenawa, *Cancer Science*, 2005, **96**, 379–386.
67 A. E. Pelling, F. S. Veraitch, C. P.-K. Chu, C. Mason and M. A. Horton, *Cell Motil. Cytoskeleton*, 2009, **66**, 409–422.
68 J. G. Goetz, S. Minguet, I. Navarro-Lérida, J. J. Lazcano, R. Samaniego, E. Calvo, M. Tello, T. Osteso-Ibáñez, T. Pellinen, A. Echarri, A. Cerezo, A. J. P. Klein-Szanto, R. Garcia, P. J. Keely, P. Sánchez-Mateos, E. Cukierman and M. A. Del Pozo, *Cell*, 2011, **146**, 148–163.
69 M. Krieg, G. Fläschner, D. Alsteens, B. M. Gaub, W. H. Roos, G. J. L. Wuite, H. E. Gaub, C. Gerber, Y. F. Dufrêne and D. J. Müller, *Nat Rev Phys*, 2019, **1**, 41–57.
70 S. Iyer, R. M. Gaikwad, V. Subba-Rao, C. D. Woodworth and I. Sokolov, *Nature Nanotech*, 2009, **4**, 389–393.
71 I. Sokolov, S. Iyer, V. Subba-Rao, R. M. Gaikwad and C. D. Woodworth, *Appl. Phys. Lett.*, 2007, **91**, 023902.
72 P.-H. Wu, D. R.-B. Aroush, A. Asnacios, W.-C. Chen, M. E. Dokukin, B. L. Doss, P. Durand-Smet, A. Ekpenyong, J. Guck, N. V. Guz, P. A. Janmey, J. S. H. Lee, N. M. Moore, A. Ott, Y.-C. Poh, R. Ros, M. Sander, I. Sokolov, J. R. Staunton, N. Wang, G. Whyte and D. Wirtz, *Nat Methods*, 2018, **15**, 491–498.
73 N. W. Tschoegl, .
74 W. N. Findley, J. S. Lai and K. Onaran, *Creep and relaxation of nonlinear viscoelastic materials: with an introduction to linear viscoelasticity*, Dover, New York, 1989.
75 Y. M. Efremov, W.-H. Wang, S. D. Hardy, R. L. Geahlen and A. Raman, *Sci Rep*, 2017, **7**, 1541.
76 E. A. López-Guerra and S. D. Solares, *Beilstein J. Nanotechnol.*, 2014, **5**, 2149–2163.
77 E. A. López-Guerra, B. Eslami and S. D. Solares, *J. Polym. Sci. Part B: Polym. Phys.*, 2017, **55**, 804–813.
78 C. H. Parvini, M. A. S. R. Saadi and S. D. Solares, *Beilstein J. Nanotechnol.*, 2020, **11**, 922–937.
79 C. H. Parvini, A. X. Cartagena-Rivera and S. D. Solares, *Commun Biol*, 2022, **5**, 17.
80 B. Uluutku, E. A. López-Guerra and S. D. Solares, *Beilstein J. Nanotechnol.*, 2021, **12**, 1063–1077.
81 B. Uluutku, M. R. McCraw and S. D. Solares, *Journal of Applied Physics*, 2022, **131**, 165101.
82 M. McCraw, B. Uluutku and S. Solares, *Rep. Mech. Eng.*, 2021, **2**, 156–179.
83 A. Chandrashekar, A. Givois, P. Belardinelli, C. L. Penning, A. M. Aragón, U. Staufer and F. Alijani, , DOI:10.48550/ARXIV.2206.04017.
84 K. Vemaganti, S. Madireddy and S. Kedari, *Mech Time-Depend Mater*, 2020, **24**, 1–24.
85 A. Bonfanti, J. L. Kaplan, G. Charras and A. Kabla, *Soft Matter*, 2020, **16**, 6002–6020.
86 S. Moreno-Flores, R. Benitez, M. dM Vivanco and J. L. Toca-Herrera, *Journal of Biomechanics*, 2010, **43**, 349–354.
87 P. O. J. Scherer, *Computational physics: simulation of classical and quantum systems*, Springer, Berlin Heidelberg, 2010.
88 I. J. Myung, *Journal of Mathematical Psychology*, 2003, **47**, 90–100.
89 J. I. Myung and M. A. Pitt, *Psychological Review*, 2009, **116**, 499–518.
90 J. Mulder and W. J. van der Linden, *Psychometrika*, 2009, **74**, 273–296.
91 K. Fujita, K. Okada and K. Katahira, *The Fisher information matrix: A tutorial for calculation for decision making models*, PsyArXiv, 2022.
92 J. Andere-Rendon, D. C. Montgomery and D. A. Rollier, *Journal of Quality Technology*, 1997, **29**, 451–463.

93 A. C. Atkinson, *Journal of Statistical Planning and Inference*, 2008, **138**, 56–64.
94 S. L. Brunton and J. N. Kutz, *Data-driven science and engineering: machine learning, dynamical systems, and control*, Cambridge University Press, Cambridge, 2019.
95 N. Chacko, M. Liebling and T. Blu, *J. Opt. Soc. Am. A*, 2013, **30**, 2012.
96 C. Sötebier, A. Michel and J. Fresnais, *Applied Sciences*, 2012, **2**, 485–495.
97 Z. Wang, A. A. Volinsky and N. D. Gallant, *J. Appl. Polym. Sci.*, 2014, **131**, n/a-n/a.
98 A. Mata, A. J. Fleischman and S. Roy, *Biomed Microdevices*, 2005, **7**, 281–293.
99 M. Rubinstein and R. H. Colby, *Polymer physics*, Oxford University Press, Oxford ; New York, 2003.
100 J. S. de Sousa, J. A. C. Santos, E. B. Barros, L. M. R. Alencar, W. T. Cruz, M. V. Ramos and J. Mendes Filho, *Journal of Applied Physics*, 2017, **121**, 034901.
101 B. R. Brückner, H. Nöding and A. Janshoff, *Biophysical Journal*, 2017, **112**, 724–735.
102 B. Xu, H. Li and Y. Zhang, *Biomatter*, 2013, **3**, e24651.
103 T. Indei and J. Takimoto, *The Journal of Chemical Physics*, 2010, **133**, 194902.
104 P. C. Cai, B. Su, L. Zou, M. J. Webber, S. C. Heilshorn and A. J. Spakowitz, *ACS Cent. Sci.*, 2022, **8**, 1318–1327.
105 P. C. Cai, B. A. Krajina and A. J. Spakowitz, *Phys. Rev. E*, 2020, **102**, 020501.
106 J. E. Sader, J. W. M. Chon and P. Mulvaney, *Review of Scientific Instruments*, 1999, **70**, 3967–3969.